


Biochar for supercapacitor electrodes: Mechanisms in aqueous electrolytes

Caiyu Ma¹ | Longnian Tang¹ | Haiyun Cheng¹ | Zhuangnan Li² |
Wenyao Li^{1,3} | Guanjie He³ 

¹School of Materials Science and Engineering, Mechanical Industrial Key Laboratory of Boiler Low-Carbon Technology, Shanghai University of Engineering Science, Shanghai, China

²Department of Materials Science and Metallurgy, University of Cambridge, Cambridge, UK

³Electrochemical Innovation Lab, Department of Chemical Engineering, University College London, London, UK

Correspondence

Wenyao Li and Guanjie He,
Electrochemical Innovation Lab,
Department of Chemical Engineering,
University College London, London WC1E
7JE, UK.
Email: liwenyao314@gmail.com and
g.he@ucl.ac.uk

Funding information

Major Research Plan,
Grant/Award Number: 62374107; National
Natural Science Foundation of China,
Grant/Award Number: 62374107;
Shanghai Local Universities Capacity
Building Project of Science and
Technology Innovation Action Program,
Grant/Award Number: 21010501700; Class
III Peak Discipline of Shanghai-Materials
Science and Engineering; Engineering and
Physical Sciences Research Council,
Grant/Award Numbers: EPSRC, EP/
V027433/3; EPSRC Centre for Doctoral
Training in Molecular Modelling and
Materials Science, Grant/Award Number:
EP/L015862/1; UK Research and
Innovation (UKRI) Under the UK
Government's Horizon Europe Funding,
Grant/Award Numbers: 101077226, EP/
Y008707/1

Abstract

The utilization of biomass materials that contain abundant carbon–oxygen/nitrogen functional groups as precursors for the synthesis of carbon materials presents a promising approach for energy storage and conversion applications. Porous carbon materials derived from biomass are commonly employed as electric-double-layer capacitors in aqueous electrolytes. However, there is a lack of detailed discussion and clarification regarding the kinetics analysis and energy storage mechanisms associated with these materials. This study focuses on the modification of starch powders through the KOH activation process, resulting in the production of porous carbon with tunable nitrogen/oxygen functional groups. The kinetics and energy storage mechanism of this particular material in both acid and alkaline aqueous electrolytes are investigated using in situ attenuated total reflectance-infrared in a three-electrode configuration.

KEYWORDS

biomass carbon, electrode, in situ ATR-IR, supercapacitor

This is an open access article under the terms of the [Creative Commons Attribution](https://creativecommons.org/licenses/by/4.0/) License, which permits use, distribution and reproduction in any medium, provided the original work is properly cited.

© 2024 The Authors. *Battery Energy* published by Xijing University and John Wiley & Sons Australia, Ltd.

1 | INTRODUCTION

The goal of achieving the peak of carbon dioxide emissions and striving to achieve carbon neutralization are both a responsibility and mission for humans, as well as an opportunity and a challenge. Electrochemical energy storage devices have been developed accordingly, with the aim of achieving a carbon-neutral fuel cycle and limiting carbon dioxide emissions to the atmosphere.^{1–3} Among various electrochemical energy storage technologies, supercapacitors (SCs) are regarded as one of the most promising candidates for high-power and long-cycle life energy storage devices.^{4,5} According to different charge storage mechanisms, two types of SCs were classified, that is, electric-double-layer capacitors (EDLCs) and pseudocapacitors.^{6,7} The differences between the two types are the charge storing by ion adsorption/desorption or surface redox reactions.⁸ Currently, there are many low-cost biomass wastes that have been used to generate electrode materials for EDLCs. Compared with fossil-based materials, biomass carbon materials are environmentally friendly and have sustainable advantages as well as promising commercial prospects.^{9–14} To achieve high properties, a detailed understanding of the interactions between the electrolyte and electrode materials and the charge storage mechanism of SCs during electrochemical processes is required. Besides traditional characterization techniques to reveal the evolution such as morphological and structural transformation, and so forth,¹⁵ novel in situ techniques have been employed to explore the dynamic charge storage process of SCs.^{16,17}

Till now, the energy storage mechanism and electrochemical reaction process of SCs with different materials are still not fully understood. In situ techniques such as in situ X-ray diffraction (in situ XRD), in situ Raman, in situ nuclear magnetic resonance (in situ NMR), and so forth have been used to extract information on crystal structures, physicochemical properties, and correlate them with electrochemical properties to explore electrochemical mechanisms.^{18–21} Among them, in situ NMR has been widely studied to explore ion diffusion and charge storage mechanisms in SCs. For example, John M. Griffin et al. used in situ NMR in the electrolyte tetraethyltetrafluoroborate in acetonitrile to directly quantify the amount of anionic and cationic species within a working microporous carbon SC electrode and found that the charge storage mechanisms are different. For positive polarization, charging occurs by cation–anion exchange, while for negative polarization, cation adsorption predominates.²² Alexander C. Forse et al. used in situ pulsed field gradient NMR spectroscopy to directly measure ion diffusion in SCs. It was found that electrolyte concentration and carbon pore size distribution also affect intrapore diffusion and the movement of carbon ions into and out of nanopores.²³ These physicochemical

characterizations and studies convey information about the Faradaic and non-Faradic mechanism in SCs, and the behavior of electrolyte ion transport under operating conditions. In particular, specific in situ testing methods have certain limitations. For example, in situ XRD is not suitable for amorphous electrode materials; the interaction of in situ atomic force microscope tips and electrode materials generates the interference of the electrochemical reactions.^{17,24} However, in situ Raman and in situ attenuated total reflectance-infrared (in situ ATR-IR) have the flexibility and accuracy to explore the relationships between reaction intermediates and molecule structures during the reaction, which have become important methods to explore the mechanisms of the charge storage.^{25,26} Especially, the in situ infrared radiation (in situ IR) technique offers an effective method to identify molecular-level changes in electrochemical reactions, which can provide more evidence to support pseudocapacitive reaction mechanisms in SCs.²⁷ Moreover, in situ IR technology has played an indispensable role in studying the microstructure and chemical reaction mechanism of materials in recent years in the fields of energy, environment and catalysis.^{28–31} In the previous studies on the energy storage mechanism of SCs, in situ Raman was used to explore the relationship between electrode materials and electrolytes based on the change of the polarizability of vibration materials.^{26,32–34} But the study of electrochemical processes by in situ IR has been rarely reported. In a reported work on the electrochemical mechanism of SCs' detection with in situ ATR-IR techniques, Richey et al. investigated the ionic dynamics of EMIm-TFSI in electrodes made of porous carbide-derived carbon and nonporous onion-like carbons. They detected cations and anions enter and leave the carbide-derived carbon pores during charging and discharging.³⁵ Wang et al. successfully clarify the charge storage mechanism of the MOF-PC (metal organic framework derived porous carbon) cathode of Zn-based hybrid SC (i.e., MOF-PC//Zn) by using in situ ATR-IR analysis in a nonaqueous electrolyte (0.5 M Zn-TFMS in dimethylformamide solution), which is found that the charge storage mechanism mainly based on the anions/cations adsorption and exchange in macropores.³⁶ These studies are based on the ionic kinetic mechanism of EDLCs with organic or ionic liquids as electrolytes. However, so far, the reports on the ionic dynamics mechanism of biomass carbon materials containing N and O functional groups in SCs in aqueous electrolytes and the chemical changes at the molecular level in electrochemical energy storage have not been revealed in detail.

Herein, N, O-co-doped biomass carbon materials were prepared by a simple one-step annealing. As SC electrodes, high specific capacitances and extraordinary stabilities were obtained. Furthermore, the chemical changes at the molecular level during electrochemical energy storage

in acidic (0.5 M H₂SO₄) and alkaline electrolytes (1 M KOH) are revealed by in situ ATR-IR technology. Additionally, this in situ technology revealed the molecular bonding and breaking and the change of functional groups of biomass carbon material SCs during the electrochemical process in aqueous electrolytes, which provides direct evidence of molecular-level chemical changes. This is of great significance for the exploration of the energy storage mechanism of SCs.

2 | EXPERIMENTAL

2.1 | Materials synthesis

The mixture of potato starch, urea, and KOH powders with different mass ratios (potato starch:urea:KOH powders = 1:3:3, 1:3:6, or 1:3:9) was ground and annealed for carbonization at different temperatures (700°C, 800°C, or 900°C). For the convenience of distinguishing materials of different proportions, their abbreviations are shown in Table 1. The as-obtained samples were dispersed in 3 M HCl solution and washed with DI water subsequently. Finally, the purified porous carbon was freeze-dried for further use.

2.2 | Material characterization

The morphology of the carbon was detected by scanning electron microscope (SEM; S-4800) and transmission electron microscopy (JEOL, JEM-2100) equipped with an energy-dispersive X-ray spectrometer. The chemical

TABLE 1 Abbreviation of samples synthesized at different temperatures with mixtures of potato starch, urea, and potassium hydroxide powders in different mass ratios.

Sample abbreviation	Potato starch (mass ratio)	Urea (mass ratio)	KOH (mass ratio)	<i>T</i> (°C)
BC-133-7	1	3	3	700
BC-133-8	1	3	3	800
BC-133-9	1	3	3	900
BC-136-7	1	3	6	700
BC-136-8	1	3	6	800
BC-136-9	1	3	6	900
BC-139-7	1	3	9	700
BC-139-8	1	3	9	800
BC-139-9	1	3	9	900

compositions were recorded by the X-ray photoelectron spectroscopy (XPS; Thermo Scientific K-alpha photoelectron spectrometer), ATR-IR spectroscopy, and Raman spectroscopy (Renishaw Raman microscope spectrometer with the laser wavelength of 514.5 nm). Nitrogen adsorption–desorption isotherms were measured at 77 K (Quantachrome Autosorb-iQC), and the Brunauer–Emmett–Teller (BET) method was used to identify the specific surface area.

2.3 | Electrochemical performance

The electrochemical performance was evaluated in a three-electrode configuration. The as-synthesized carbon powers were mixed with 10% of polyvinylidene difluoride in *N*-methyl-2-pyrrolidone solution to form a slurry and paste onto the cleaned carbon papers (~1 cm × 4 cm) with an area of 1 cm². The electrodes were further dried under vacuum at 110°C. The loading mass density was controlled by 1–2 mg cm⁻². During the electrochemical performance test, Ag/AgCl electrode, Pt plate electrode, and as-prepared electrode were used as reference, counter, and working electrode, respectively. In addition, 1 M KOH or 0.5 M H₂SO₄ was used as the electrolytes. The corresponding formulas for calculating specific capacitance are provided in the Supporting information.

2.4 | In situ ATR-IR measurements

A Bruker Tensor 27 IR vacuum ATR-IR spectrometer with a diamond crystal single-reflection internal reflection element ATR prism was used for recording IR spectra. The instrument is equipped with a room temperature DLATGS detector with a resolution of 4 cm⁻¹. In this experiment, a three-electrode system was used to test the in situ ATR-IR spectroscopy of the SC during the reaction. The reference electrode (RE) was Ag/AgCl, and the counter electrode (CE) was a Pt sheet. After clamping, let the SC with an aqueous acid–base electrolyte equilibrate the potential (deoxygenated for 20 min prior with Ar) before applying the voltage. Electrochemical measurements were performed using a PalmSens Emstat2 potentiostat (PalmSens). After acquiring the IR background spectrum at open circuit potential, the potential is applied and the spectrum is recorded relative to that of the equilibrium sample. The applied potential was adjusted from –1 to 1 V with respect to RE in steps of –0.05 V. Each spectrum was recorded after holding a specific potential for 10 min. All spectra were corrected for background subtraction of ATR crystal spectra.

3 | RESULTS AND DISCUSSION

Raman spectroscopy is an indispensable detection method to discover the disordered structures in sp^2 carbon materials. The Raman spectra (Figure 1A) of the obtained biomass carbon materials reveal two intense bands at 1385 and 1592 cm^{-1} , which correspond to the D-peak and G-peak, respectively. The D-peak reflects the defect of the materials, which is directly proportional to the intensity, and the G-band is related to the first-order scattering of the tensile vibration mode E_{2g} in sp^2 carbon. Therefore, the ratio of D-peak and G-peak can be utilized to judge the perfection of the carbon structure. From Figure 1A, it can be seen that the ratios of the D-peak to the G-peak of the biomass carbon materials annealed at different temperatures are all less than 1, which indicates a high degree of graphitization. When the carbonization temperatures were 700°C , 800°C , and 900°C , the ratios of D-peak to G-peak were 0.703, 0.843, and 0.828, respectively. Different ratios of D-peak to G-peak indicate that biomass carbon has different structures and pore size distribution. This result

demonstrates that the biomass carbon annealed at 800°C contains higher porosity, and it has more active sites that can participate in electrochemical reactions. Figure 1B shows the SEM image of BC-136-8 biomass carbon material. (The upper right corner is the image at high magnification.) It can be seen that the material has a honeycomb-like morphology. To obtain thinner pore walls and larger specific surface area, it can usually be treated by adding KOH. The magnified electron microscope image shows that tiny pores are also present in the carbon skeleton. More active sites are provided for the capacitors. SEM images of different ratios of biomass carbon materials at different annealing temperatures are shown in Supporting Information S1: Figure S1–S3. Figure 1C shows the TEM image of the biomass carbon annealed at 800°C , that is, BC-136-8. The material presents a uniform amorphous structure and porous microstructure, a certain number of irregular mesopores, and these massive worm-like micropores facilitate fast ion diffusion and charge transfer, thereby enhancing the performance of SCs. This is in good agreement with the morphology observed in SEM images (Supporting

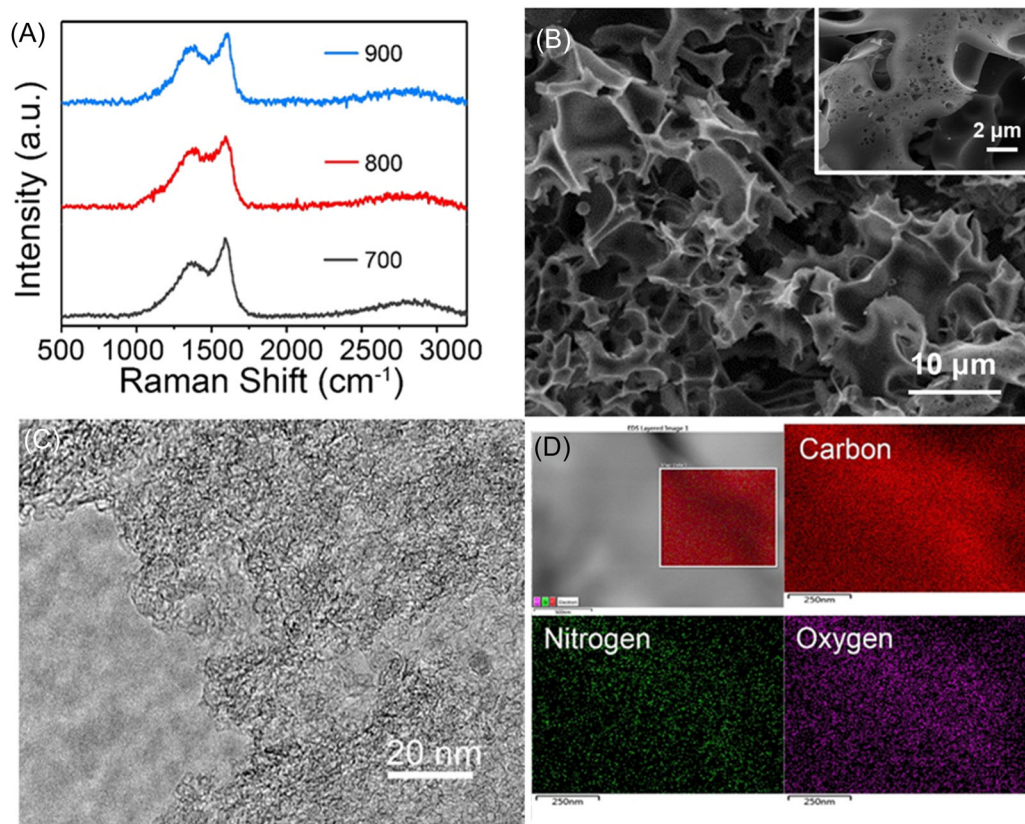


FIGURE 1 (A) Raman spectra of BC-136 annealed at different temperatures; (B) scanning electron microscope images of BC-136-8 electrode material with different magnification ratios; (C) transmission electron microscopy image of the BC-136 annealed at the temperature of 800°C ; (D) scanning transmission electron microscopy image recorded by the high angle annular dark field detector. Energy dispersive spectrometer maps of mixed elements, carbon, nitrogen, and oxygen, respectively.

Information S1: Figure S1–S3). Further, the chemical compositions of biomass carbon by scanning transmission electron microscopy-energy dispersive spectrometer (STEM-EDS) are analyzed. The EDS element mapping in Figure 1D shows the distribution of C, N, and O in the composite, and the weight percentage of the elements obtained by EDS is 89.12% C, 6.09% N, and 4.79% O. The element content of carbon materials annealed at different

temperatures with different ratios are shown in Supporting Information S1: Table S1–3 and Figure S4. This shows that the biomass materials were successfully doped with N and O elements, and each element in the composite material was evenly distributed.

The BET-specific surface area of different biomass carbon obtained through variable conditions is shown in Figure 2A. Among them, samples 1–3 represent biomass

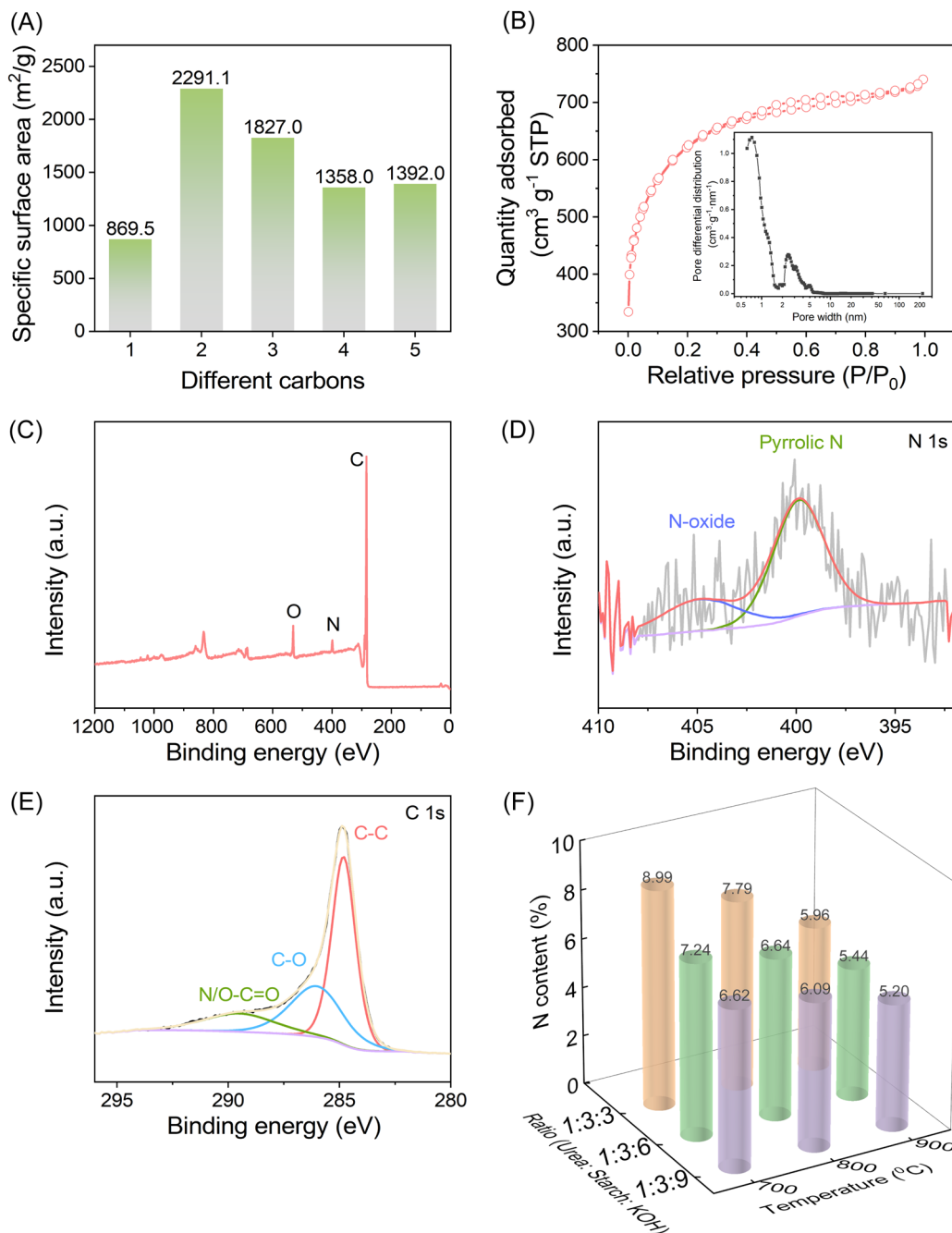


FIGURE 2 (A) Brunauer–Emmett–Teller surface areas of different biomass carbons obtained via variable conditions, the sample numbers of 1–5 are BC-136-7, BC-136-8, BC-136-9, BC-133-8, and BC-139-8, respectively; (B) N₂ adsorption–desorption isotherms of BC-136-8; inset showing pore size distribution of the material; X-ray photoelectron spectroscopy (XPS) spectra of (C) wide XPS and (D) N 1s and (E) C 1s spectra, respectively; (F) ratio of N elements under different ratios and annealing temperatures.

carbon materials with the same mass ratio (BC-136), and the specific surface areas of biomass carbon materials prepared at different annealing temperatures (700°C, 800°C, and 900°C). When the annealing temperature is 800°C, the specific surface area reaches 2267 m² g⁻¹, which is the highest among samples 1–3. In addition, three samples 2, 4, and 5 represent the specific surface area of biomass carbon materials with different mass ratios under the same annealing temperature of 800°C (BC-136-8, BC-133-8, BC-139-8). In addition, the specific surface area comparison of biomass carbon materials annealed at different temperatures with different ratios is shown in Supporting Information S1: Figure S5. Among these, the specific surface area of the BC-136-8 is still the largest.

The adsorption curve of Figure 2B clearly shows that the BC-136-8 has a type I isotherm (IUPAC classification), indicating the microporous feature. Normally, the characteristics of the hysteresis loop correspond to different pore structures. This biomass carbon also exhibits a representative H4-type hysteresis loop at P/P_0 from 0.3 to 0.9, which corresponds to the adsorption behavior of a mixture of microporous and mesoporous materials. The hysteresis in the isotherm is usually related to the capillary aggregation in the mesoporous structure and is also affected by the adsorbent and the adsorption environment. This also can be supported by the nonlocal density functional theory pore size distribution in the inset of Figure 2B. The pore distribution peaks of the sample are all between 0.5 and 8 nm, indicating that the materials have formed micropores and smaller mesopores. Depending on the isotherm, the BET total pore volume of the biomass carbon is calculated as 1.07205 cm³ g⁻¹. In addition, it proved that biomass carbon has a strong adsorption potential.

The as-prepared biomass carbon material BC-136-8 was further characterized by XPS. In this work, the biomass carbon material mainly contains carbon and a small amount of nitrogen and oxygen. In addition, the C 1s spectrum of the biomass carbon material (Figure 2E) is deconvoluted into three peaks at 284.82, 286.03, and 289.63 eV, corresponding to C–C, C–O, and N/O–C=O, respectively. The strong peak of sp^2 is located at 284.82 eV, indicating a high degree of graphitization of conjugated sp^2 in the as-prepared biomass carbon, which is in good agreement with the Raman analysis. The N 1s spectrum (Figure 2D) shows that two peaks are located at 400.68 and 405.2 eV, which correspond to pyrrole–N and N–O bonds, respectively. Among them, pyrrole–N is known as the main nitrogen component that contributes to the pseudocapacitance. It is expected that the combined action of nitrogen and oxygen functional groups on the carbon surface will accumulate more defects and larger active sites for charge storage during

the redox reaction. Besides, the N and O functional groups on the surface of biomass carbon can provide good wettability for the electrode material, increasing the surface area accessible to ions,^{37,38} which could increase the hydrophilicity of carbon materials and improve the polarity of the materials.³⁹ It is conducive to the rapid penetration of electrolyte ions into the internal structures and reduces diffusion resistance.⁴⁰ Figure 2C shows the broad spectrum of the XPS of BC-136-8, which has peaks at 284.8, 400, and 532.8 eV for C, N, and O, respectively. In addition, Figure 2f shows the highest elemental N content in three different proportions of biomass carbon materials under annealing temperatures. As the annealing temperature increases, the elemental N content of the material decreases. Furthermore, at the same temperature, the elemental N content decreases when the proportion of KOH doping increases. From the above results it can be seen that the content of element N in the material is closely related to the annealing temperature and the amount of KOH doping.

Figure 3 shows the cyclic voltammetry (CV) and galvanostatic charge/discharge (GCD) curves of BC-136-8 biomass carbon materials with annealing temperature of 800°C under acidic and alkaline electrolytes, respectively. The GCD curve of the material presents a symmetrical triangular shape, and the CV diagram presents an approximately rectangular shape, which indicates that the material has excellent electrochemical performance and excellent capacitive performance. At the current density of 0.5 A g⁻¹, the specific capacitance is 727.6 F g⁻¹ for an electrolyte of 0.5 M H₂SO₄ and 460.99 F g⁻¹ for an electrolyte of 1 M KOH. The electrochemical performance of BC-136-8 is the best, which is better than that of the biomass carbon material with the same current density in other reports. (This is due to the low charge transfer resistance of the electrode material BC-136-8. The corresponding Nyquist diagram is shown in Supporting Information S1: Figure S5.) The electrochemical performances of biomass carbon materials at different current densities with annealing temperatures of 700°C, 800°C, and 900°C at various ratios are shown in Supporting Information S1: Figures S6 and S7. In addition, the specific capacitance at 800°C for electrode materials with different proportions is calculated and presented in Supporting Information S1: Figure S8. It is obvious that the sample BC-136-8 exhibits better rate performance due to larger and more stable specific capacitance in 0.5 M H₂SO₄ electrolyte and 1 M KOH electrolyte.

To understand the electrochemical performance of the BC-136-8 electrode materials, 1 M KOH aqueous solution and 0.5 M H₂SO₄ were used as electrolytes, and a three-electrode cell was used for measurements. The

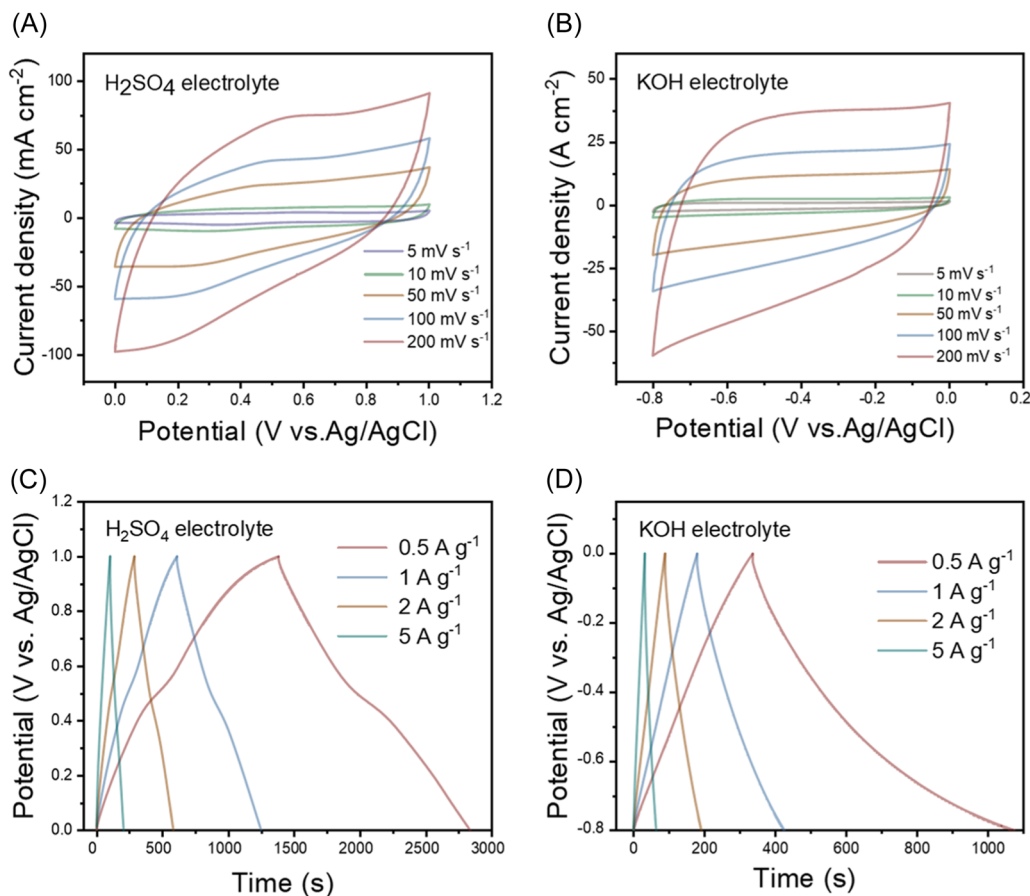


FIGURE 3 (A) and (B) are the cyclic voltammetry plots of BC-136-8 electrode material in H_2SO_4 electrolyte and KOH electrolyte, respectively. (C) and (D) are the galvanostatic charge/discharge curves of BC-136-8 electrode material in H_2SO_4 and KOH electrolytes, respectively.

results within the potential range of -0.8 to 0 V (vs. Ag/AgCl) are defined in Figure 4A. In addition, the red shaded area corresponds to the surface capacitance contribution, with a contribution ratio of 88.2%. At a scan rate of 20 mV s^{-1} , the obtained CV curve has almost no redox peaks, showing a nearly rectangular shape. This shows that the material exhibits ideal EDLC during charging and discharging. Similarly, with $0.5 \text{ M H}_2\text{SO}_4$ aqueous solution as the electrolyte, the CV result measured under a three-electrode system is shown in Figure 4B. At a scan rate of 20 mV s^{-1} , a typical CV curve is shown within the potential window of 0 to 1 V. The surface-controlled contribution is 79.1%. The contribution rate of pseudocapacitance is attributed to the surface of the biomass carbon material doped with N/O functional groups. Figure 4C shows the cycling stability of the BC-136-8 electrode in a three-electrode system with 1 M KOH and $0.5 \text{ M H}_2\text{SO}_4$ electrolytes. Under a scan rate of 100 mV s^{-1} , after 50,000 times CV cycles, the capacitance has nearly no attenuation with the 1 M KOH electrolyte, and the 50,000th CV curve completely overlaps the first cycle, indicating that the electrode

material has extraordinary excellent cycling performance. Besides, when the electrolyte changes to $0.5 \text{ M H}_2\text{SO}_4$, the capacitance can reach 92.1% retention of its initial value after 50,000 times cycles. The inset CV curves show that redox peaks appear after 50,000 times tests compared with the first time, because the doping of N and O atoms will involve electrochemical reactions on the surface contributing to the pseudocapacitance. The good capacitance retention proves that the biomass carbon material has robust electrochemical performance and can be used as an ideal energy electrode material.

To understand the charge storage mechanism of the biomass carbon as the electrode, in situ ATR-IR spectroscopy was adopted to directly detect the evolution in the structure of the biomass carbon electrode material during the electrochemical process by the infrared spectrum reflection of the N, O-doped biomass carbon. Figure 5A shows the in situ ATR-IR test results of BC-136-8 electrode in a three-electrode testing system from -0.1 to -1 V under an alkaline condition (1 M KOH). The absorption peak at 1643.2 cm^{-1} is attributed to the C=O stretching vibration peak. However, there is a

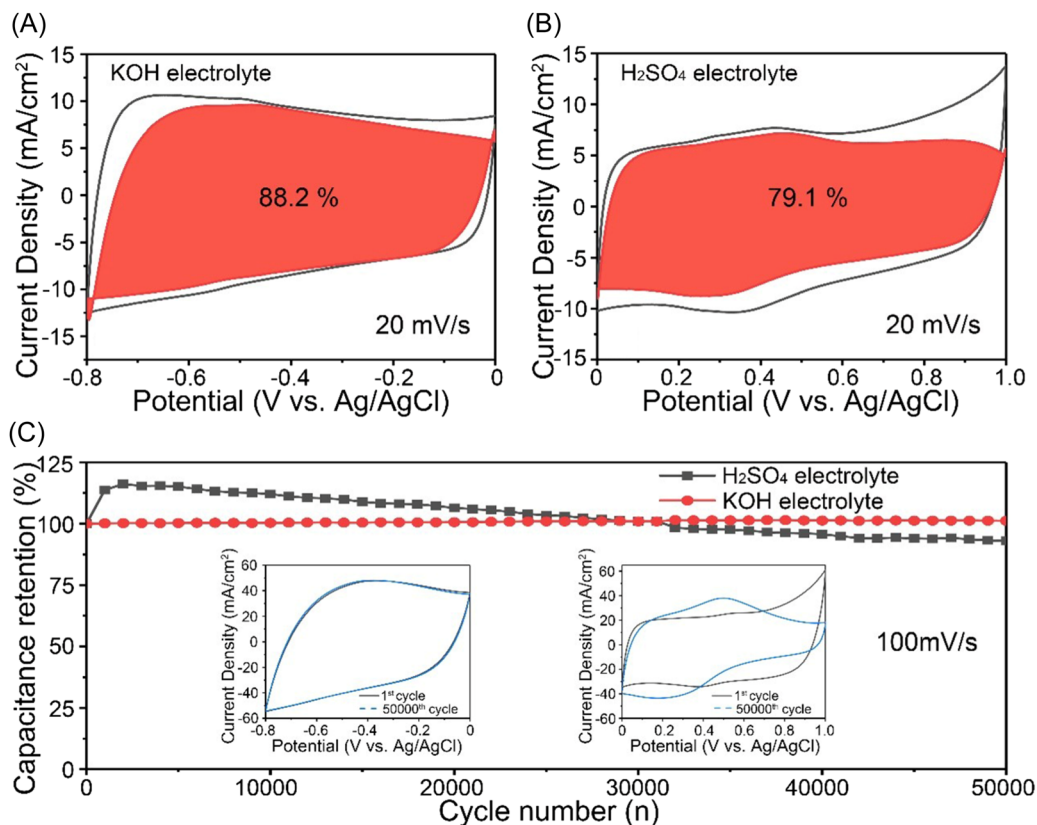


FIGURE 4 Separation of capacitive and diffusive currents measured at 20 mV s^{-1} for biomass carbon materials BC-136-8 in (A) KOH and (B) H_2SO_4 electrolytes: total current (black line) and capacitive current (red shaded); (C) cycling performance of the electrodes in different electrolytes, that is, acid and base solution, and cyclic voltammetry (CV) curves for the first cycle and the 50,000th cycle in two electrolytes, that is, base solution on the left and acid solution on the right.

strong absorption peak at 3390.6 cm^{-1} , which is attributed to the stretching vibration of the $-\text{OH}$ group. In the alkaline electrolyte, the content of hydroxyl groups increases with the depth of the discharge process, which is attributed to the fact that the $\text{C}-\text{O}$ functional groups can combine with the reduced H^+ in the electrolyte to form $\text{C}-\text{OH}$ bonds on the surface of carbon materials and generate a large number of OH^- groups simultaneously (reaction are presented in right down of Figure 5B). In the KOH electrolyte, the main charge storage mode of SCs in aqueous electrolytes is to store electric charges. In addition, the N, O-doped biomass carbon materials can provide pseudocapacitance through the redox reaction of carbonyl or quinoid groups. In addition, the use of in situ ATR-IR technology revealed the chemical changes at the molecular level during the electrochemical process, providing direct evidence for the charge storage mechanism of SCs previously studied.

The in situ ATR-IR test of the BC-136-8 material using $0.5 \text{ M H}_2\text{SO}_4$ as the electrolyte was conducted, as shown in Figure 5C. Within the potential range of $0-1 \text{ V}$, there are two functional groups that are positively increasing along with the increase of potential. They

are the $\text{C}=\text{O}$ stretching vibration peak at 1650.9 cm^{-1} and the $-\text{OH}$ stretching vibration peak at 3433.0 cm^{-1} , respectively. During the charging process, the $\text{C}-\text{C}$ bonds on the surface of the biomass-derived material are cleaved and then bond with hydroxyl groups and oxygen- or nitrogen-containing functional groups. During this process, a redox reaction occurs, and finally $\text{N}/\text{O}-\text{C}=\text{O}$ bonds are formed. This is consistent with the results in the XPS test. In addition, due to the redox reaction between the $\text{C}=\text{O}$ functional group on the surface of the carbon material and the free H^+ in the acidic electrolyte during the charging process, a $\text{C}-\text{OH}$ bond is formed (reaction equation is presented in the right down of Figure 5D). The intermolecular redox reaction induces the stretching vibration of the OH^- bond, and the peak of the $-\text{OH}$ functional group gradually increases. Also, during charging, there are some absorption peaks that are retrorsely increasing with increasing potential. For example, there are small sharp absorption peaks at 1074.3 and 1253.6 cm^{-1} . This is due to the bending vibration of $\text{C}-\text{O}-\text{C}$, which is oxidized to $\text{C}=\text{O}$ groups during charging, thus its content decreases with increasing potential. The opposite absorption peaks

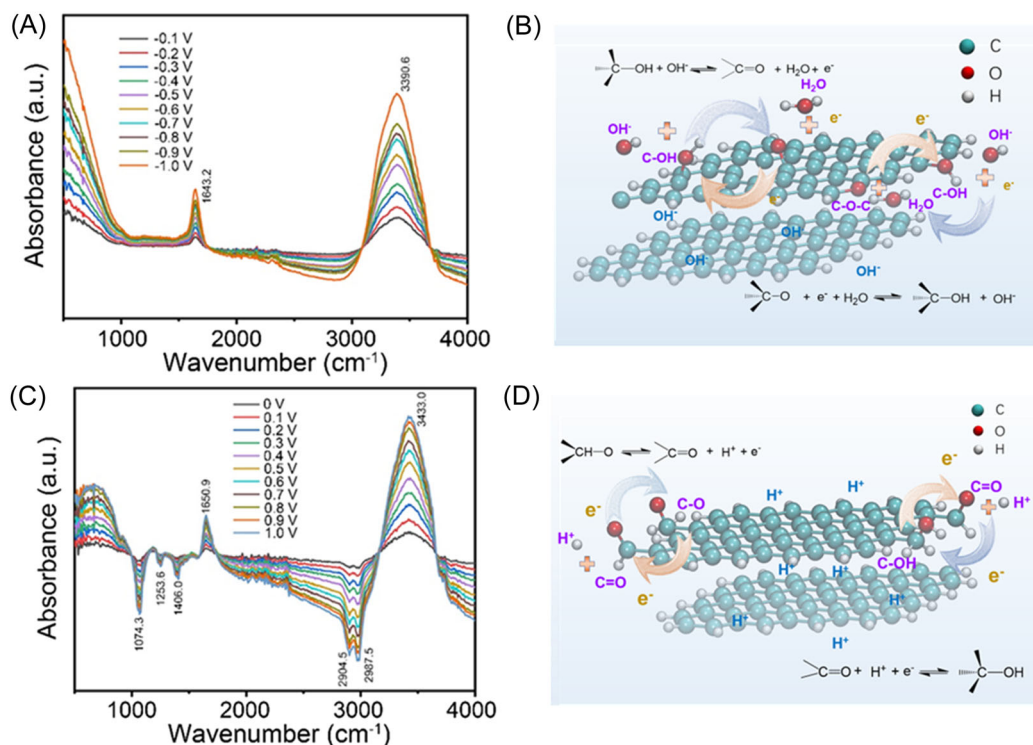


FIGURE 5 In situ attenuated total reflectance-infrared spectra of electrode materials in (A) KOH and (C) H₂SO₄ electrolytes. Electrochemical reaction process diagram of electrode materials in (B) KOH and (D) H₂SO₄ electrolytes.

TABLE 2 Electrochemical properties of the materials compared with those previously reported electrode materials based on biomass carbon materials in supercapacitors for comparison.

No.	Biomass precursor	Electrolyte type	Current density (A g ⁻¹)	Cs (F g ⁻¹)	Number of cycles	Reference
1	Pumpkin-derived	1 M NaSO ₄	1	419	10,000	[41]
2	<i>Cajanus cajan</i> stems	1 M KOH	2.5	126	50,000	[42]
3	Bean sprouts	0.5 M H ₂ SO ₄	1	204	2000	[12]
4	Porous carbon nanosheets	1 M KOH	1	407	50,000	[43]
5	Cotton stalk	1 M KOH	20	528	1000	[44]
6	Biomass sorghum seeds	6 M KOH	0.5	537	15,000	[45]
7	Pomelo peel	1 M H ₂ SO ₄	1	209	10,000	[46]
8	Stiff silkworm	6 M KOH	1	304	4000	[47]
9	Sub-1-nm pore-rich carbon	1 M KOH	1	299	10,000	[48]
10	<i>Perilla frutescens</i>	1 M NaSO ₄	2	270	10,000	[13]
11	Coconut shells	1 M H ₂ SO ₄	1	258	3000	[49]
12	Regenerated silk fibroin	1 M H ₂ SO ₄	1	264	10,000	[39]
13	Coal and biomass carbon	1 M KOH	1	354	1000	[50]
14	Ginkgo leaves	1 M H ₂ SO ₄	0.5	374	2000	[9]
15	Biomass carbon	0.5 M H ₂ SO ₄	0.5	727	50,000	This work
		1 M KOH	1	461	50,000	

at 2904.5 and 2987.5 cm^{-1} are caused by the bending vibration of C–H, and they generally appear as doublets. Due to the reduction reaction of the aldehyde group H–C=O during the charging process, the chemical bond is broken to generate carbonyl and hydrogen ions (reactions are presented in the left upper part of Figure 5D). Hydrogen adsorbs on the surface of the material and can provide additional pseudocapacitance during redox processes (Table 2).

By comparing with those previously reported electrode materials based on biomass carbon materials in SCs, it can be seen that the N and O-co-doped biomass carbon materials prepared in this work have better electrochemical performance and longer cycle life.

4 | CONCLUSIONS

In summary, we successfully prepared N, O-co-doped biomass carbon electrode material by using potato starch as the precursor and urea as a nitrogen source. It is found that the electrode exhibits a high specific capacitance (i.e., 460.99 F g^{-1} in 1 M KOH and 727.6 F g^{-1} in 0.5 M H_2SO_4 electrolytes at 0.5 A g^{-1} , respectively) and extraordinary excellent long-life stability of 50,000 cycles, that is, the capacitance retentions of 100% in 1 M KOH and 92.1% in 0.5 M H_2SO_4 electrolytes, respectively. Importantly, by using in situ ATR-IR analysis, we successfully clarified the charge storage mechanism of biomass carbon electrode material under two aqueous electrolytes (i.e., 1 M KOH and 0.5 M H_2SO_4) and explored the storage capacity of SCs from the concentration of functional groups and the bonding and breaking of molecules at the molecular level. From the in situ ATR-IR results, it can be clearly detected that the redox processes of carbonyl or quinoid groups would occur to provide pseudocapacitance in an alkaline electrolyte. Compared with alkaline electrolytes, the formation and breaking of more complex chemical bonds are involved in acidic electrolytes. Not only reversible electrochemical reactions occur among H–C–O groups, C=O groups and C–OH groups, but also a reversible process of breaking and forming C–O–C bonds and C–H bonds. In addition, hydrogen atoms adsorbed on the surface of carbon materials can undergo redox reactions, providing additional pseudocapacitance.

ACKNOWLEDGMENTS

This work was financially supported by the National Natural Science Foundation of China (Grant No. 62374107), Shanghai Local Universities Capacity Building Project of Science and Technology Innovation Action Program (21010501700), Class III Peak Discipline of

Shanghai-Materials Science and Engineering (High-Energy Beam Intelligent Processing and Green Manufacturing), and Engineering and Physical Sciences Research Council (EPSRC, EP/V027433/3), EPSRC Centre for Doctoral Training in Molecular Modelling and Materials Science (EP/L015862/1), UK Research and Innovation (UKRI) Under the UK Government's Horizon Europe funding (101077226, EP/Y008707/1).

CONFLICT OF INTEREST STATEMENT

The authors declare no conflict of interest.

DATA AVAILABILITY STATEMENT

The data supporting the findings of this study are available within the article or its supplementary materials.

ORCID

Guanjie He  <http://orcid.org/0000-0002-7365-9645>

REFERENCES

- Zhou Q, Li X, Ouyang S. Carbon-neutral organisms as the new concept in environmental sciences and research prospects. *J Agro-Environ Sci.* 2022;41(1):1-9.
- Gani A. Fossil fuel energy and environmental performance in an extended STIRPAT model. *J Clean Prod.* 2021;297:126526.
- Lieberei J, Gheewala SH. Resource depletion assessment of renewable electricity generation technologies-comparison of life cycle impact assessment methods with focus on mineral resources. *Int J Life Cycle Assess.* 2017;22(2):185-198.
- Merin P, Joy PJ, Muralidharan MN, Gopalan EV, Seema A. Biomass-derived activated carbon for high-performance supercapacitor electrode applications. *Chem Eng Technol.* 2022;45(4):649-657.
- Fic K, Platek A, Piwek J, Frackowiak E. Sustainable materials for electrochemical capacitors. *Mater Today.* 2018;21(4):437-454.
- Wang Y, Zhang L, Hou H, et al. Recent progress in carbon-based materials for supercapacitor electrodes: a review. *J Mater Sci.* 2021;56(1):173-200.
- Saini S, Chand P, Joshi A. Biomass derived carbon for supercapacitor applications: review. *J Energy Storage.* 2021;39:102646.
- Shaker M, Ghazvini AAS, Cao W, Riahifar R, Ge Q. Biomass-derived porous carbons as supercapacitor electrodes—a review. *New Carbon Mater.* 2021;36(3):546-572.
- Zhu X, Yu S, Xu K, et al. Sustainable activated carbons from dead ginkgo leaves for supercapacitor electrode active materials. *Chem Eng Sci.* 2018;181:36-45.
- Wong MH, Ok YS, Naidu R. Biological—waste as resource, with a focus on food waste. *Environ Sci Pollut Res.* 2016;23(8):7071-7073.
- Bi Z, Kong Q, Cao Y, et al. Biomass-derived porous carbon materials with different dimensions for supercapacitor electrodes: a review. *J Mater Chem A.* 2019;7(27):16028-16045.

12. Cao X, Li Z, Chen H, et al. Synthesis of biomass porous carbon materials from bean sprouts for hydrogen evolution reaction electrocatalysis and supercapacitor electrode. *Int J Hydrogen Energy*. 2021;46(36):18887-18897.
13. Liu B, Liu Y, Chen H, Yang M, Li H. Oxygen and nitrogen co-doped porous carbon nanosheets derived from *Perilla frutescens* for high volumetric performance supercapacitors. *J Power Sources*. 2017;341:309-317.
14. Momodu D, Okafor C, Manyala N, Bello A, ZebazeKana MG, Ntsoenzok E. Transformation of plant biomass waste into resourceful activated carbon nanostructures for mixed-assembly type electrochemical capacitors. *Waste Biomass Valorization*. 2019;10(6):1741-1753.
15. Kumar S, Saeed G, Zhu L, Hui KN, Kim NH, Lee JH. 0 D to 3D carbon-based networks combined with pseudocapacitive electrode material for high energy density supercapacitor: a review. *Chem Eng J*. 2021;403:126352.
16. Patra A, K. N, Jose JR, Sahoo S, Chakraborty B, Rout CS. Understanding the charge storage mechanism of supercapacitors: in situ/operando spectroscopic approaches and theoretical investigations. *J Mater Chem A*. 2021;9(46):25852-25891.
17. Chen J, Lee PS. Electrochemical supercapacitors: from mechanism understanding to multifunctional applications. *Adv Energy Mater*. 2021;11(6):2003311.
18. Kim J, Kim E, Lee U, et al. Nondisruptive in situ Raman analysis for gas evolution in commercial supercapacitor cells. *Electrochim Acta*. 2016;219:447-452.
19. Krittayavathananon A, Pettong T, Kidkhunthod P, Sawangphruk M. Insight into the charge storage mechanism and capacity retention fading of MnCo_2O_4 used as supercapacitor electrodes. *Electrochim Acta*. 2017;258:1008-1015.
20. Seema R, Mandal S, Singh P, Paul S, Chanda N. Fiber Bragg grating sensors for in-situ temperature measurement on bending a flexible planar supercapacitor. *Sens Actuator A*. 2020;314:112266.
21. Wang H, Köster TKJ, Trease NM, et al. Real-time NMR studies of electrochemical double-layer capacitors. *J Am Chem Soc*. 2011;133(48):19270-19273.
22. Griffin JM, Forse AC, Tsai WY, Taberna PL, Simon P, Grey CP. In situ NMR and electrochemical quartz crystal microbalance techniques reveal the structure of the electrical double layer in supercapacitors. *Nat Mater*. 2015;14(8):812-819.
23. Forse AC, Griffin JM, Merlet C, et al. Direct observation of ion dynamics in supercapacitor electrodes using in situ diffusion NMR spectroscopy, nature. *Energy*. 2017;2(3):7.
24. Du YM, Zhang YF, Zhang CH, Liu YP. In situ nanoindentation mechanical property of films by atomic force microscope. *Rare Metal Mater Eng*. 2015;44(8):1959-1963.
25. Chen CG, Song MY, Lu LZ, Yue LJ, Huang T, Yu AS. Application of in situ Raman and Fourier transform infrared spectroelectrochemical methods on the electrode-electrolyte interface for lithium-oxygen batteries. *Batteries Supercaps*. 2021;4(6):850-859.
26. Chen XY, Cheng Y, Matsuba M, et al. In situ monitoring of heterogeneous hydrosilylation reactions using infrared and Raman spectroscopy: normalization using phase-specific internal standards. *Appl Spectrosc*. 2019;73(11):1299-1307.
27. Cave EA, Olson JZ, Schlenker CW. Ion-pairing dynamics revealed by kinetically resolved in situ FTIR spectroelectrochemistry during Lithium-Ion storage. *ACS Appl Mater Interfaces*. 2021;13(41):48546-48554.
28. Mozhzhukhina N, Tesio AY, De Leo LPM, Calvo EJ. In situ infrared spectroscopy study of PYR14TFSI ionic liquid stability for Li-O₂ battery. *J Electrochem Soc*. 2017;164(2):A518-A523.
29. Zhao Y, Chen Z. Application of Fourier transform infrared spectroscopy in the study of atmospheric heterogeneous processes. *Appl Spectrosc Rev*. 2010;45(1):63-91.
30. Chen Y, Zou C, Mastalerz M, Hu S, Gasaway C, Tao X. Applications of micro-Fourier transform infrared spectroscopy (FTIR) in the geological sciences—a review. *Int J Mol Sci*. 2015;16(12):30223-30250.
31. Gao F, Tian XD, Lin JS, Dong JC, Lin XM, Li JF. In situ Raman, FTIR, and XRD spectroscopic studies in fuel cells and rechargeable batteries. *Nano Research*. 2023;16(4):4855-4866.
32. Chen DC, Xiong XH, Zhao BT, Mahmoud MA, El-Sayed MA, Liu ML. Probing structural evolution and charge storage mechanism of NiO_2H_x electrode materials using in operando resonance Raman spectroscopy, advanced. *Science*. 2016;3(6):1500433.
33. Yang L, Cheng S, Ji X, Jiang Y, Zhou J, Liu M. Investigations into the origin of pseudocapacitive behavior of Mn_3O_4 electrodes using in operando Raman spectroscopy. *J Mater Chem A*. 2015;3(14):7338-7344.
34. Chen D, Ding D, Li X, et al. Probing the charge storage mechanism of a pseudocapacitive MnO_2 electrode using in operando Raman spectroscopy. *Chem Mater*. 2015;27(19):6608-6619.
35. Richey FW, Dyatkin B, Gogotsi Y, Elabd YA. Ion dynamics in porous carbon electrodes in supercapacitors using in situ infrared spectroelectrochemistry. *J Am Chem Soc*. 2013;135(34):12818-12826.
36. Qiu X, Wang N, Wang Z, Wang F, Wang Y. Towards high-performance zinc-based hybrid supercapacitors via macropores-based charge storage in organic electrolytes. *Angew Chem Int Ed*. 2021;60(17):9610-9617.
37. Butsyk O, Olejnik P, Romero E, Plonska-Brzezinska ME. Postsynthetic treatment of carbon nano-onions: surface modification by heteroatoms to enhance their capacitive and electrocatalytic properties. *Carbon*. 2019;147:90-104.
38. Mirzaeian M, Abbas Q, Hunt MRC, Hall P. Pseudocapacitive effect of carbons doped with different functional groups as electrode materials for electrochemical capacitors. *Energies*. 2020;13(21):5577.
39. Yun YS, Cho SY, Shim J, et al. Microporous carbon nanoplates from regenerated silk proteins for supercapacitors. *Adv Mater*. 2013;25(14):1993-1998.
40. Yang J, Zhou X, Wu D, Zhao X, Zhou Z. S-doped N-rich carbon nanosheets with expanded interlayer distance as anode materials for sodium-ion batteries. *Adv Mater*. 2017;29(6):1604108.
41. Bai S, Tan G, Li X, et al. Pumpkin-derived porous carbon for supercapacitors with high performance. *Chem Asian J*. 2016;11(12):1828-1836.
42. Byatarayappa G, Guna V, Venkatesh K, Reddy N, Nagaraju N, Nagaraju K. Superior cycle stability performance of a symmetric coin cell fabricated using KOH activated bio-char derived from agricultural waste—*Cajanus cajan* stems. *J Environ Chem Eng*. 2021;9(6):106525.
43. Chen C, Yu D, Zhao G, et al. Three-dimensional scaffolding framework of porous carbon nanosheets derived from plant

- wastes for high-performance supercapacitors. *Nano Energy*. 2016;27:377-389.
44. Fang K, Chen M, Chen J, Tian Q, Wong CP. Cotton stalk-derived carbon fiber@Ni-Al layered double hydroxide nanosheets with improved performances for supercapacitors. *Appl Surf Sci*. 2019;475:372-379.
 45. Feng T, Wang S, Hua Y, et al. Synthesis of biomass-derived N,O-codoped hierarchical porous carbon with large surface area for high-performance supercapacitor. *J Energy Storage*. 2021;44:103286.
 46. Fu G, Li Q, Ye J, et al. Hierarchical porous carbon with high nitrogen content derived from plant waste (pomelo peel) for supercapacitor. *J Mater Sci*. 2018;29(9):7707-7717.
 47. Gong C, Wang X, Ma D, Chen H, Zhang S, Liao Z. Microporous carbon from a biological waste-stiff silkworm for capacitive energy storage. *Electrochim Acta*. 2016;220:331-339.
 48. Jiang Y, Chen J, Zeng Q, et al. Facile method to produce sub-1 nm pore-rich carbon from biomass wastes for high performance supercapacitors. *J Colloid Interface Sci*. 2022;612:213-222.
 49. Sun K, Leng C, Jiang J, et al. Microporous activated carbons from coconut shells produced by self-activation using the pyrolysis gases produced from them, that have an excellent electric double layer performance. *New Carbon Mater*. 2017;32(5):451-459.
 50. Zhang X, Sun B, Fan X, et al. Hierarchical porous carbon derived from coal and biomass for high performance supercapacitors. *Fuel*. 2022;311:122552.

SUPPORTING INFORMATION

Additional supporting information can be found online in the Supporting Information section at the end of this article.

How to cite this article: Ma C, Tang L, Cheng H, Li Z, Li W, He G. Biochar for supercapacitor electrodes: mechanisms in aqueous electrolytes. *Battery Energy*. 2024;20230058.
[doi:10.1002/bte2.20230058](https://doi.org/10.1002/bte2.20230058)